

JPL Document D-66100

TECHNOLOGY DEVELOPMENT FOR EXOPLANET MISSIONS

**Assessing the performance limits of internal
coronagraphs through end-to-end modeling**

Technology Milestone #1 Whitepaper

**John Krist, PI
Ruslan Belikov
Dimitri Mawet
Dwight Moody
Laurent Pueyo
Stuart Shaklan
John Trauger**

7 July 2010

National Aeronautics and Space Administration

Jet Propulsion Laboratory
California Institute of Technology
Pasadena, California

© 2011. All rights reserved.

Assessing the performance limits of internal coronagraphs

Approvals

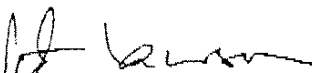
Released by



John E. Krist,
Principal Investigator

2 August 2010

Approved by



Peter R. Lawson,
Exoplanet Program Chief Technologist, JPL

8/2/2010



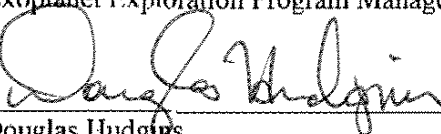
Marie Levine,
Exoplanet Program Technology Facilities Manager, JPL

8/2/2010



Michael Devirian
Exoplanet Exploration Program Manager, JPL

8-2-10



Douglas Hudgins
Exoplanet Exploration Program Scientist, NASA HQ

8/2/10



Lia LaPiana
Exoplanet Exploration Program Executive, NASA HQ

8/2/10

Assessing the performance limits of internal coronagraphs

Table of Contents

1. Objective	1
2. Introduction	1
2.1. Exoplanet imaging	1
2.2. Coronagraphs	2
2.2.1 Phase induced amplitude apodization (PIAA) coronagraph	2
2.2.2 Vector vortex coronagraph (VVC)	4
2.2.3 Hybrid band-limited coronagraph (HBLC)	5
2.3. Coronagraph numerical models	6
2.4. Goals of this study	8
2.5. Application to future NASA missions	8
2.6. Modeling framework	8
2.7. Caveats	9
3. Milestone #1 Description	10
3.1. Milestone Prerequisites	10
3.1.1 Coronagraph contrast and image plane field dimensions	10
3.1.2 Optical system layout	10
3.1.3 PIAA	10
3.1.4 VVC	11
3.1.5 HBLC	11
3.2. Milestone Requirements	11
3.2.1 Algorithm efficiency	11
3.2.2 Algorithm accuracy	12
3.3. Milestone Metrics	13
3.3.1 Algorithm efficiency	13
3.3.2 Algorithm accuracy	14
4. Success Criteria	15
5. Milestone Certification Data Package	16
6. References	17
Appendix A: Optical system layout	19
Appendix B: PIAA modeling and verification	21
Appendix C: VVC modeling and verification	23
Appendix D: HBLC modeling and verification	27

Assessing the performance limits of internal coronagraphs

TDEM Milestone #1 White Paper: Assessing the Performance Limits of Internal Coronagraphs Through End-to-End Modeling

1. Objective

In support of NASA's Exoplanet Exploration Program and the ROSES Technology Development for Exoplanet Missions (TDEM), this whitepaper explains the purpose of the TDEM Milestone #1 for developing and verifying modeling algorithms for selected internal coronagraphs. It specifies the methodology for computing the milestone's metrics, and establishes the success criteria against which the milestone will be evaluated.

This study is in preparation for Milestone #2, which will be an assessment of the theoretical performance limits of the selected coronagraphs in a system with realistic optical aberrations as derived through end-to-end modeling. That milestone will use the algorithms developed and verified in Milestone #1 to characterize the wavefront control behavior of each coronagraph and identify the limiting factors for achieving 10^{-10} contrast over a broad bandpass for future coronagraphic missions. Milestone #2 will be described in a subsequent document.

2. Introduction

The technology milestone described here serves to gauge the developmental progress of optical modeling for a space-based coronagraphic mission such as ACCESS (Trauger et al. 2008) or the Terrestrial Planet Finder Coronagraph (TPF-C; Traub et al. 2006) that would detect and characterize exoplanets. Completion of this milestone is to be documented in a report by the Principal Investigator and reviewed by NASA HQ.

2.1. Exoplanet imaging

A mission like ACCESS or TPF-C must be able to detect a planet whose apparent brightness relative to the star is on the order of 10^{-9} (Jupiter-like) to 10^{-10} (Earth-like) at visible wavelengths. For even a nearby system such a planet would be seen at a small angle from the star. Diffracted and scattered light from even the feasibly best space telescope would overwhelm the feeble signal from the planet at these small separations. The diffracted light can be significantly reduced using a coronagraph, which is an optical component that specifically filters the wavefront to remove the light from the central source (star). However, unavoidable optical fabrication errors (e.g. imperfect polishing and non-uniform coatings) will scatter light that the coronagraph cannot suppress. Wavefront control using one or more deformable mirrors can largely compensate for these errors.

The coronagraph and the wavefront control system operate together to create a *dark hole* centered on the image of the star to enable observation of an exoplanet. The dark hole usually begins at an inner radius where, by convention, the intensity transmission of the coronagraphic occulter is 50%. This is the *inner working angle* (IWA). Depending on the coronagraph design, the practical limit to the IWA is between $2 \lambda/D$ to $4 \lambda/D$ radians (D is the telescope diameter; hereafter, angles expressed as multiples of λ/D will be in radians). The *outer working angle* (OWA) is the outer radius of the dark hole and is limited by the number of deformable mirror (DM) actuators, N , that map across the pupil diameter. The maximum dark hole radius is $(N/2) \lambda/D$ at the shortest wavelength in the passband.

The light level in the dark hole is defined in terms of its *contrast*. The broadband contrast is the ratio of the average (across the bandpass) scattered starlight level in the dark hole to the average (again over the bandpass) peak light level of an image of the star when the coronagraph mask (which blocks the starlight at the image plane) is removed. In other words, it is the brightness of a field point source, relative to the star, whose peak is equal in intensity to the mean dark hole brightness.

2.2. Coronagraphs

There are a wide variety of coronagraphs. Three of the most studied of those proposed for space missions are the hybrid band-limited coronagraph (HBLC; Moody et al. 2008), the vector vortex coronagraph (VVC; Mawet et al. 2009a), and the phase-induced amplitude apodization (PIAA; Guyon et al. 2005) coronagraph. To suppress diffraction, each modifies the wavefront in a different manner: in the focal plane, the VVC primarily affects phase (via polarization manipulation) and the HBLC alters amplitude and phase, while PIAA geometrically remaps the wavefront at the pupil to create an apodized beam. All three have been tested in the High Contrast Imaging Testbed (HCIT; Trauger et al. 2007) at the Jet Propulsion Laboratory down to contrast levels (monochromatic light, one-half dark hole, one deformable mirror) of 5×10^{-10} (HBLC with a linear occulter), 2×10^{-7} (VVC; Mawet 2009b), and 4×10^{-7} (PIAA, with the deformable mirror after the beam is remapped; Kern et al. 2009, Belikov et al. 2009). Given that these methods alter the wavefront in vastly different ways, one may expect that they have different sensitivities to the aberrations present in any optical system.

2.2.1 Phase induced amplitude apodization (PIAA) coronagraph

Apodization of a telescope pupil will produce a point spread function with significantly reduced wing intensity, making it a technique of interest for high contrast imaging. Conventional apodizers using transmission-altering masks reduce throughput too much to be acceptable for exoplanet imaging, and they would be difficult to accurately fabricate and operate over broad bandpasses. As an alternative method of apodization, PIAA utilizes two optics (lenses or mirrors) that geometrically distort the wavefront. The first optic, M1, is located at a pupil and remaps the beam onto the second optic, M2, which corrects for the phase errors from the remapping to create a “flat” wavefront (see Figure 1).

Pure PIAA systems that provide 10^{-10} contrast are impractical due to diffraction effects and stringent surface tolerances. These can be reduced in a hybrid system by using a weak apodizer (*post-apodizer*) placed near or at a subsequent image of M2 (Pluzhnik et al. 2006a, 2006b). In practice, post-apodizers are implemented using binary transmission masks composed of a series of narrow, opaque rings spaced and sized to provide the desired diffraction reduction. These have been fabricated using lithographic techniques (Kern et al. 2009).

After the post-apodizer the beam is brought to a focus where an occulting spot masks the central lobe of the apodized stellar point spread function (PSF). At this point any field sources are highly distorted and blurred. To restore the original wavefront mapping and thus image quality, the beam is fed through an identical set of PIAA optics, but in reverse order (no apodizer is required for the reverse system).

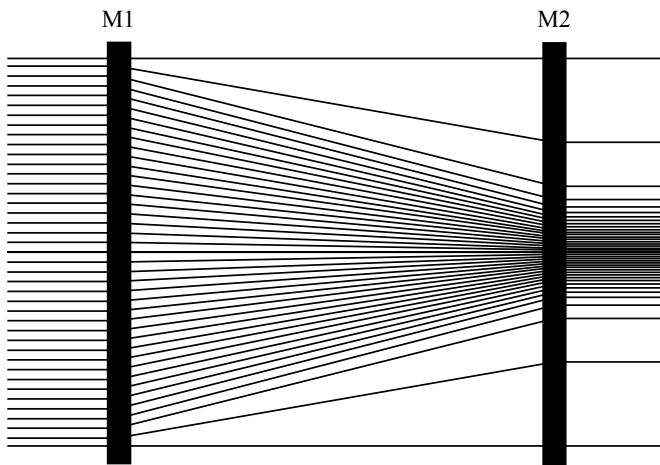


Figure 1. Schematic ray diagram showing how the PIAA M1 optic creates an apodized beam. The beam remains collimated at the very edge during propagation, but towards the center it becomes compressed. The PIAA M2 optic corrects for phase distortions introduced by the remapping.

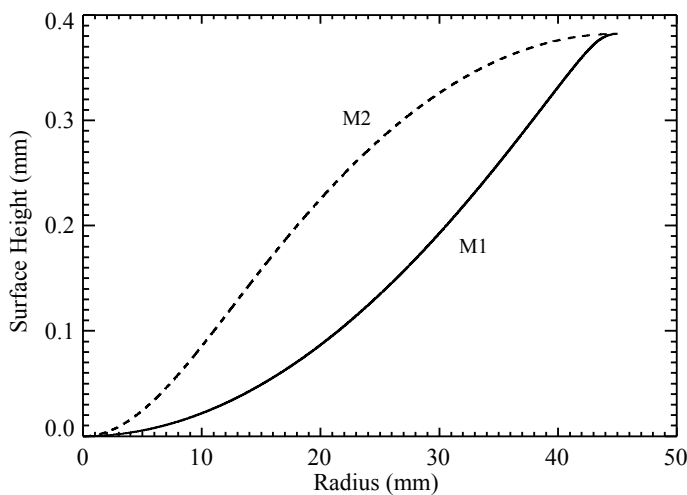


Figure 2. Surface height profiles of a set of PIAA optics (90 mm diameter, 900 mm separation). Note that the Y axis is magnified compared to the X axis.

2.2.2 Vector vortex coronagraph (VVC)

An optical vortex is created using a mask that introduces an azimuthally-varying phase shift to the wavefront, creating a “phase screw” with a singularity at the center. This results in self-interference as the wavefront propagates, forming a dark central hole in the beam at some distance from the mask. An optical vortex can be used in a Lyot coronagraph by placing a vortex-generating mask at an intermediate image plane that results in a dark central hole at a subsequent pupil plane, where a Lyot stop is placed. The advantages of an optical vortex coronagraph are that it can provide imaging very close to the star ($< 2 \lambda/D$), has high throughput ($>90\%$) due to a relatively wide-open Lyot stop, and is tolerant of low-order aberrations (depending on the design).

Previous vortex masks were transmissive, stepped spiral patterns etched into substrates. They suffered from manufacturing defects due to the imperfect singularity at the center of the spiral and the small, nanometer-scale steps required to produce an approximation to a smooth phase ramp. They were also inherently chromatic.

A new technique (Mawet et al. 2009a) has been developed that creates a “geometrical” phase spiral by manipulating the polarization of incoming light with novel coatings made of hardened birefringent liquid crystal polymers (LCPs). This *vector vortex* is nothing more than a rotationally symmetric halfwave plate (HWP) providing a geometrical phase shift that applies opposite phase screws to the two orthogonal circular polarization states (Fig. 3). In the vector vortex, for a linearly polarized input field (or for natural light projected onto a linear basis), the rotationally symmetric HWP rotates the polarization vector as in Fig. 3a. The definition of circular polarization is a linear polarization rotating at the angular frequency ω (equal to that of the electromagnetic field); a rotation $\varphi = 2\theta$ of the polarization vector is strictly equivalent to a phase delay (Fig. 3b). If, at any given point in space, the polarization vector is rotated such as in Fig. 3a, it implies that the given circular polarization (Fig. 3b) has acquired a geometric phase ramp $e^{i\varphi} = e^{i2\theta}$ such as that represented in Fig. 3c. The term φ thus represents both an angle and a phase – hence the term “geometrical” phase.

The details of this technique are given by Mawet (2009a). This form, called the vector vortex coronagraph (VVC), has many advantages over the physical vortex mask. Very smooth and accurate phase ramps can be created, and with multilayer coatings it can be made fairly achromatic. It does, however, require a small circular mask ($r < 0.5 \lambda/D$) to cover manufacturing errors at the singularity. Depending on the *charge* of the vortex (the number of waves the phase ramp goes through - 4 to 6 is practical), the inner working angle is $1.8 \lambda/D - 2.4 \lambda/D$. A significant disadvantage is the inability to create a dark hole simultaneously for both orthogonal polarizations.

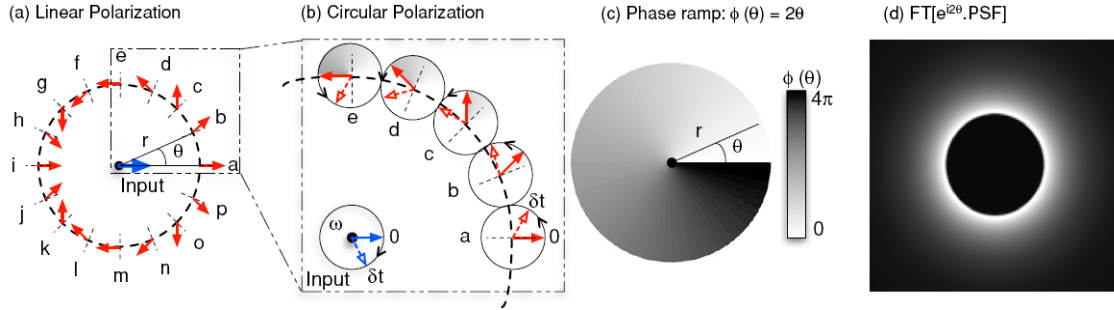


Figure 3. The VVC azimuthal phase ramp. Panel A: rotationally symmetric HWP with an optical axis orientation that rotates about the center (dashed lines perpendicular to the circumference). The net effect of a HWP on a linear impinging polarization is to rotate it by $-2 \times \alpha$ where α is the angle between the incoming polarization direction and the fast optical axis. An incoming horizontal polarization (blue arrow) is transformed by the vector vortex so that it spins around its center twice as fast as the azimuthal coordinate θ (red arrows). Panel B: for circular polarization, the output field rotation is strictly equivalent to a phase delay (the starting angle 0 is rotated; therefore phase shifted). The angle of local rotation of the polarization vector corresponds to a “geometrical” phase: upon a complete rotation about the center of the rotationally symmetric HWP, it has undergone a total $2 \times 2\pi$ phase ramp, which corresponds to the definition of an optical vortex of topological charge 2 (panel C). Upon propagation from the focal plane to the subsequent pupil plane, the Fourier transform (FT) of the product of the PSF by the azimuthal phase ramp sends the light outside the original pupil area (Panel D).

2.2.3 Hybrid band-limited coronagraph (HBLC)

The HBLC is a variation of the classical Lyot coronagraph having an occulting mask at a focus that blocks the central portion of the stellar point spread function. A graded transmission mask is used for very high contrast imaging as it provides for better diffraction suppression than a solid occulter (Kuchner & Traub 2002). At a subsequent image of the entrance pupil a simple aperture mask, the Lyot stop, blocks light along the outer edge of the beam. The stop diameter is sized specifically to the occulter; the smaller the occulter is, the smaller the Lyot stop clear aperture is.

A graded-transmission occulter can be created using a variable-thickness layer of a metal, and such occulters have been used successfully in the HCIT (Trauger et al. 2007). This coating introduces wavelength-dependent transmission and phase shifts that are dependent on the layer thickness and material properties. Careful selection of materials can reduce these effects; nickel, for instance, offers a favorable relationship between refractive indices and wavelength (Balasubramanian 2008), providing useful and nearly constant optical depths across the visible spectrum. To partly compensate for the phase dispersion over a broad wavelength range, multilayer variable-thickness dielectric coatings are deposited on top of the transmission pattern or on the back side of the substrate (Figure 4).

With realistic materials and number of coating layers, the HBLC mask and Lyot stop cannot achieve a band-limited, 20% broadband contrast of 10^{-10} without additional wavefront modification provided by deformable mirrors. The DMs, focal plane mask, and

Lyot stop are all considered as part of the coronagraph. The DM settings required to achieve the required performance are derived using an iterative wavefront control algorithm and an unaberrated, simulated layout.

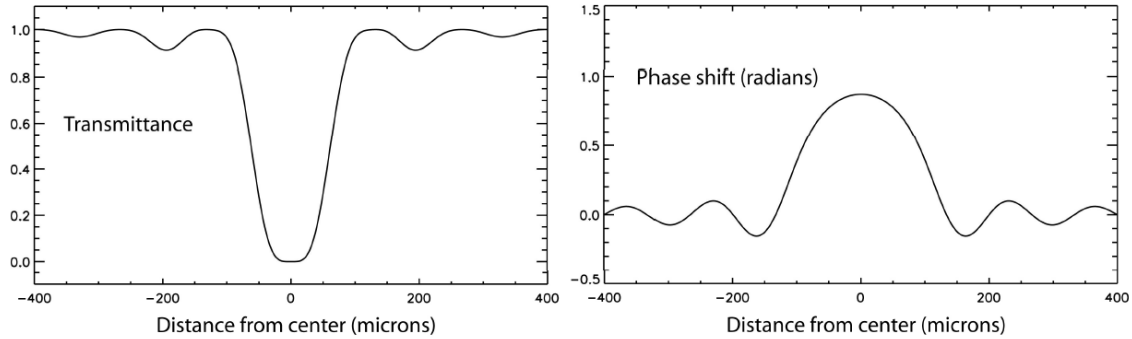


Figure 4. Attenuation and phase shift profiles for a 4th order linear occulter HBLC mask with an inner working angle of $3 \lambda/D$. From Moody et al. (2008).

2.3. Coronagraph numerical models

Accurate wavefront propagation methods are needed to derive the behavior and performance of a coronagraph in a realistic system (Krist et al. 2006, 2009). They can also be used to investigate data analysis techniques prior to obtaining real data (Krist et al. 2008). Purely analytical models may sometimes be useful for initial performance estimates in the absence of aberrations or other system defects, but they are usually impractical for predicting what happens for realistic systems. For those cases, accurate numerical propagation modeling techniques are required to predict real-world performance.

In addition to performance predictions, propagation models are needed to build the deformable mirror response matrix that is used for wavefront control (Give'on et al. 2007). This contains the predicted changes in the electric field in the image plane produced by motion of each DM actuator. The wavefront control algorithm uses it to determine the DM settings that minimize the starlight inside the dark hole. It is generated by applying a small piston to each actuator in a system model and computing the resulting field. Using two 48×48 actuator DMs with five sensing wavelengths (to provide a broadband solution), the number of image plane fields that must be computed is over 18,000. Even when the problem is reduced in number by invoking symmetry (if possible), the number of propagations is over 2,000. Rigorous diffraction algorithms such as Rayleigh-Sommerfeld take days to propagate just one wavefront, and even if they took just an hour, it would still take over three months to generate the DM response matrix. Every time the system design is altered, the matrix must be recomputed. Thus, an *accurate* and *efficient (fast)* propagator is needed for operation of the coronagraph, whether in simulation or the real world. A mission waiting for an updated response matrix would be wasting science time.

The accuracy of a propagation algorithm must be verified. This can be done either by comparing the models against results from actual hardware in a testbed or against more rigorous, physics-based algorithms or analytical representations. Of the three coronagraphs discussed here, only the band-limited coronagraph (with a linear rather than circular occulter) has achieved dark hole contrasts of 10^{-9} or better in a testbed. The VVC and PIAA have to date reached only the $\sim 10^{-7}$ level, and none in a 20% bandpass. Thus, current testbed results cannot be used to verify new modeling techniques to the 10^{-10} - 10^{-12} contrast levels required for extrasolar Earth-type planet observations.

Current modeling techniques for these coronagraphs vary in terms of efficiency, predicted accuracy, and verified accuracy. The HBLC is a modification of the amplitude-only bandlimited masks that have been evaluated in the HCIT over the past few years, including for TPF-C milestones 1 and 2 (and proposed for 3). Most of the experiments, and indeed the design of the HBLC itself, have been driven by numerical simulation (Trauger et al. 2007; Moody et al. 2008). The proprietary modeling software used, written by Dwight Moody, implements the angular spectrum and Fresnel algorithms. The model predictions agree well with the testbed results at the $\sim 10^{-9}$ level achieved on HCIT. PROPER (Krist 2007), a library of optical propagation routines that will be used in this study (Section 2.6), implements the same algorithms (and some results have been successfully compared between the two packages; note that Moody's software is not documented and not publicly available; it and PROPER have the same capabilities, with no intrinsic support for any of the coronagraphs, but PROPER is used in this study because it is publicly available and documented). Verification against rigorous methods has not been done to the 10^{-10} level. The VVC is a relatively recent development and has achieved $\sim 10^{-7}$ contrast on HCIT. The VVC was developed and its performance predicted to that level using PROPER (Mawet et al. 2009b). However, the models have not been verified in any manner (either using testbed or reference algorithms) down to 10^{-10} contrast levels, nor their speed established. Accurate models for PIAA have been developed using the S-Huygens algorithm (Vanderbei 2006; Belikov et al. 2006), but that method is too slow to be practical for repeated end-to-end modeling or DM response matrix generation (which would take over a week on a current workstation for the matrix size proposed here). In summary, there is a need for efficient algorithms whose accuracies have been verified and documented against more rigorous methods.

We note that this study will verify the efficient model accuracies against physics-based algorithms. Validation of the models (be they the efficient or rigorous ones used here) against results from actual coronagraphic hardware is required to ensure that all important properties of the system have been included. Such validation is beyond the scope of this study. The NASA Exoplanet Exploration program has a long-term goal to validate coronagraphic models against testbed results. For instance, Exoplanet Exploration Technology Milestone #3A (Shaklan 2009) has been defined to validate bandlimited coronagraph models against results in the HCIT for 10^{-9} contrast fields over a broad bandpass. The milestone document has been accepted by NASA headquarters but the project has not been funded.

Until such time that testbed validation can be done to the contrast levels of concern, verifications of practical, efficient algorithms against more rigorous ones are the only means of establishing their reliability. In the end, these new algorithms are required to

implement wavefront control on the testbeds that will be used for validation; the models will define the expected performance against which the testbed results will be judged (i.e., a testbed experiment may not achieve the performance goal set by the simulations due to misalignments or fabrication errors not included in the models). In past experience, only when a modeling algorithm has not been verified against a more thorough method will it poorly match the performance of the real system. For example, initial calculations of the performance of PIAA were done using geometrical optics, with contrast performances of $10^{-9} - 10^{-10}$ predicted; however, using more detailed modeling Vanderbei (2006) showed that diffraction effects would limit contrasts to $10^{-5} - 10^{-7}$.

2.4. Goals of this study

In this study we will develop accurate and efficient numerical propagation algorithms for the three selected coronagraphs that will be verified against rigorous analytical or numerical models. These may be used to evaluate the performance of these systems and to generate system response matrices used for wavefront control of simulated and real coronagraphs. The accuracies determined in this study can be used to assess the numerical errors on the predicted tolerances derived from future modeling efforts. These goals take the form of milestones with defined merit criteria, as described in Sections 3 and 4. The algorithms developed for each coronagraph will meet the efficiency and accuracy requirements in those milestones.

2.5. Application to future NASA missions

Any future mission that uses one of these coronagraphs will require the fast and accurate models developed in this study to

- Determine the performance of the coronagraph in real-world conditions
- Plan testbeds used to evaluate prototypes and perhaps test flight coronagraphs
- Generate the DM response matrix that is used on-orbit for determining the DM settings that produce a dark hole in the image plane around the star allowing for high contrast imaging

2.6. Modeling framework

We will use IDL (Interactive Data Language) and the PROPER optical propagation library (Krist 2007) to model the coronagraphic systems. PROPER includes routines to propagate a wavefront using Fourier-based angular spectrum and Fresnel algorithms, as well as functions to create apertures, deformable mirrors, and a variety of wavefront aberrations (both amplitude and phase). The package includes extensive documentation. New routines that will integrate with the PROPER functions will be needed to represent some of the coronagraphs. These will be written in IDL. If necessary for optimal speed, C code will be written that can be called from within the IDL/PROPER framework.

PROPER has been used for modeling of proposed space-based exoplanet missions (Krist et al. 2006, 2008, 2009). It was also used in the design and performance predictions of the NIRCcam coronagraph for the James Webb Space Telescope (Krist et al. 2007), the VVC masks made for HCIT and ground-based telescopes (Mawet et al. 2009b), the Gemini Planet Imager (Marois et al. 2008), the EPICS coronagraph on the European Extremely Large Telescope (Vérinaud et al. 2010), and the FOROS optical modeling system for SPHERE (Yaitskova et al. 2010).

The accuracy of the PROPER algorithms will be documented for the case of a simple optical system compared to a more rigorous method.

These codes will be made publicly available as an add-on package to PROPER. The system layouts and aberration maps as used in Milestone #2 that use the code developed in Milestone #1 will also be made available. This will allow the community to both use these codes for additional study of these coronagraphs and test their own coronagraphs in the same layouts to compare results.

PROPER is freely available at www.openchannelsoftware.com/projects/PROPER.

2.7. Caveats

The modeling undertaken in this study assumes scalar propagation of the wavefront. Vector propagation, which includes the physical effects of electric field interactions with conductive and non-conductive materials at small scales, is not used. Vector propagation becomes important when small apertures may act as waveguides and the electrical properties of the aperture substrate are significant (Lieber et al. 2005). In this study the impact of any vectorial effects would be mainly in the PIAA binary post-apodizer, the small occulting spot at the center of the VVC mask, and the amplitude-modifying structure of the HBLC. Based on previous studies for the Terrestrial Planet Finder Coronagraph, we expect such effects to be small as these structures are thin (i.e. we are not using thick apertures such as those used for early shaped pupil experiments). The realm of vector propagation is also well beyond the time and financial limits of this study.

3. Milestone #1 Description

We will identify, implement in code, and verify efficient numerical methods for representing wavefront modification by the Hybrid Band-Limited Coronagraph (HBLC), the Vector Vortex Coronagraph (VVC), and the Phase-Induced Amplitude Apodization (PIAA) coronagraph that are accurate to 1% or better relative to the mean field contrast for contrasts down to 10^{-10} .

3.1. Milestone Prerequisites

3.1.1 Coronagraph contrast and image plane field dimensions

All of the coronagraphic designs evaluated in this study must be capable of providing, in an aberration-free system, a mean contrast of 10^{-10} within an annulus centered on the star extending between $r = 2.5 \lambda_c/D - 18 \lambda_c/D$ in the image plane across a $\lambda = 500 - 600$ nm bandpass ($\lambda_c = 550$ nm). The inner radius is set by the occulter size and the outer radius by the expected number of deformable mirror actuators across the pupil (which will be 46 in Milestone #2) and the shortest wavelength ($18 \lambda_c/D \approx 20 \lambda/D$ at $\lambda = 500$ nm). The coronagraphs in Milestone #1 will be modeled *as designed*. Effects from chromatic leakage, phase dispersion, and other terms that are expected from the designs will be included, but manufacturing errors will not. In Milestone #2 we will evaluate systems with realistic fabrication errors and will include end-to-end modeling with wavefront control.

3.1.2 Optical system layout

The modeling algorithm for each coronagraph will be evaluated with a representation of a realistic telescope+coronagraph optical system layout derived from the ACCESS mission concept study. There are two layouts; one for PIAA and one shared by VVC and HBLC (see Appendix A). Both systems include two deformable mirrors. The DMs will only be used for the HBLC in this milestone, as that coronagraph requires them.

The layout will be represented as an unfolded (linear layout) system and implemented using the PROPER software with custom routines specific for the coronagraphs.

3.1.3 PIAA

A pupil apodization profile (including the effects of the PIAA optics and post-apodizer), A , will be chosen that produces, in an unaberrated system, a diffraction PSF that provides a contrast of 10^{-10} or better at $r_{image} \geq 2.5 \lambda_c/D$ over $\lambda=500-600$ nm. A post-apodizer of profile $A_{post-apodizer}$ will be included. The surface profile of M1 is set by $A/A_{post-apodizer}$, the distance from M1 to M2, and the diameter of the beam. The profile of M2 is then the surface that flattens the phase variations introduced by remapping and collimates the beam.

The modeling and verification process for the PIAA coronagraph is detailed in Appendix B.

3.1.4 VVC

The VVC will have a charge of 4, resulting in 4th order aberration rejection. It will have a 3-layer achromatic design optimized for the $\lambda=500-600$ nm passband. The predicted chromatic leakage term will be included. The opaque spot at the center of the screw will have a diameter of $\leq 0.5 \lambda_c/D$. This will provide an inner working angle of $1.8 \lambda_c/D$ (the coronagraph will still be evaluated at $2.5 - 18 \lambda_c/D$ like the others). A simple circular Lyot stop will be used. The results will be computed for only one polarization channel; in a dual channel system, each would have its own DMs and detector, so the performance of one channel would be the same as the other.

The modeling and verification process for the VVC is detailed in Appendix C.

3.1.5 HBLC

The HBLC used in this study will have a circular focal plane occulter that provides a 4th order (or nearly so) aberration rejection response. It will have an inner working angle of $2.5 \lambda_c/D$. A suitable occulter material will be chosen and will have a variable layer thickness set to match the desired transmission. The resulting phase shifts will be derived from thin-film calculations, as will those of the multilayer dielectric coatings used for broadband phase compensation. The Lyot stop will be a simple aperture whose opening diameter is chosen to match the filtered pupil image produced by the occulter. DM settings that provide the required broadband performance will be derived. Two DMs provide both phase and amplitude control over a full 360° field around the star (Shaklan & Green 2006).

The modeling and verification process for the HBLC is detailed in Appendix D.

3.2. Milestone Requirements

3.2.1 Algorithm efficiency

Milestone #1 Efficiency Requirement: *The efficient algorithm for each coronagraph will allow for the generation of a 2077 component (number of actuators per DM \times number of DMs \times number of sensing wavelengths) DM response matrix within 48 hours on a single modern workstation.*

Rationale:

The efficiency of the propagator is needed early on in the mission, when the dark hole is being created using an iterative control process prior to the first science observations. The initial DM matrix is typically generated using a system model with no aberrations. In some cases (testbeds and simulations) it has been seen that during the first few iterations the contrast level in the dark hole improves but then stagnates, typically when the non-linearities in the system that are not in the model begin to become apparent (e.g. modification of the DM image-plane influence functions due to unmodeled system aberrations). It is often possible to get things converging again by regenerating the DM

matrix with updated system information (e.g. phase retrieved maps of the system aberrations from on-orbit, defocused star images). If contrast is stuck at 10^{-8} and we need to get down to 10^{-10} and it takes a week to generate a new matrix, then no useful science will likely be done for that week. If it can be done in a few hours, then little of the mission lifetime is lost. Given the need for a fast turn-around to maintain observational efficiency, the numerical modeling algorithms must be fast.

As described previously, thousands of separate wavefront propagations will be required to construct the DM response matrix for either a model or real coronagraphic system having wavefront control. Given the Milestone #2 proposed convention of 46 DM actuators across the pupil, five sensing wavelengths, and invoking an 8-fold symmetrical system, we need ~ 2077 propagations through the entire system¹. The rigorous, physics-based, accurate propagation algorithms that are currently available (S-Huygens, Rayleigh-Sommerfeld) would take many days or even weeks to compute 2077 end-to-end simulations, even on multiprocessor systems. During all that time the in-space coronagraph would not be performing at its required contrast level, essentially wasting time.

To determine the 48 hour limit, the PIAA layout was implemented in PROPER, with the PIAA optics replaced with flat mirrors. Using 2048×2048 element wavefront grids, it took 43 seconds to perform one end-to-end simulation. Multiplied by 2077, it would require 24.8 hours to generate the DM response matrix. This ignores the additional time that would be required to account for propagation between actual PIAA optics. Thus, 48 hours on a single computer seems reasonable. The matrix generation process is easily parallelized, so we assume that the computation time on a single workstation can be scaled to a multi-node distributed computing system to provide an update time of a few hours or less, which agrees well with spacecraft communication intervals.

3.2.2 Algorithm accuracy

Milestone #1 Accuracy Requirement: *The efficient algorithm for each coronagraphic technique must provide an accuracy, as defined in Section 3.3.2, that is equal to or less than 1% of the mean contrast in the annulus defined in Section 3.1. The accuracy will be measured in separate simulations with aberrations chosen that produce 10^{-5} and 10^{-10} mean contrast fields (accuracies of $\leq 10^{-12}$ and $\leq 10^{-7}$ for 10^{-10} and 10^{-5} mean contrast fields, respectively).*

¹ In our hypothetical system, we use 48×48 actuator DMs with 46 actuators spaced across the projected pupil diameter. This provides $\pi(46/2)^2 = 1662$ useful actuators within the projected area of the pupil. With two DMs, the total number of actuators is 3324. We need to compute the response function for each actuator on each DM at each sensing wavelength. We assume 5 wavelengths, so a total of $3324 \times 5 = 16620$ response functions are needed. In an unaberrated, circularly-symmetric system, the response function of a DM actuator is the same as the one for an actuator on the opposite side of, and the same distance from, the DM center, with a rotation and/or transposition. We can divide the DM into 8 pie-slice sectors and compute the response functions only for the actuators in one sector. Then, we can rotate and/or transpose those functions as appropriate to create the responses for the other actuators on the DM. So, we can divide the total number of system propagations required to generate the response function matrix by 8: $16620 / 8 \approx 2077$.

Rationale:

The algorithm chosen to model a coronagraph must have sufficient accuracy to properly reflect the system's behavior in the presence of wavefront aberrations. Because scattering from individual component wavefront errors corresponding to contrasts of 10^{-11} - 10^{-12} add up to create the ensemble of light within the dark hole, the algorithms must be accurate to equivalent contrasts of 10^{-12} for fields with mean contrasts of 10^{-10} . Accuracy is also important when generating the deformable mirror response matrix used for wavefront control, which requires that the model system match the real one as close as possible - large differences will result in either a poor solution (low contrast dark hole) or divergence without any improvement. Smaller but still significant errors might allow convergence to a solution but only after many iterations.

The optical system aberrations, which correspond to power spectral density curves similar to those of actual optics, will be chosen to produce fields with these contrasts within the defined annulus.

3.3. Milestone Metrics

3.3.1 Algorithm efficiency

Milestone #1 Efficiency Metric:

The efficiency of the coronagraphic modeling algorithm is the elapsed time required to propagate one arbitrary, monochromatic wavefront from the first deformable mirror of the specified optical layout, through the optical system (including coronagraph), and then to the final image plane using a current workstation (default is a dual quad-core Xeon workstation) multiplied by the number of system propagations required to generate a DM response matrix.

Rationale:

For each coronagraph, a single wavefront will be propagated from the telescope primary mirror, through the defined optical system, and then to the final image plane using a combination of PROPER and the efficient coronagraph modeling algorithms. The elapsed time will be multiplied by 2077, the number of full system propagations required to generate the DM response matrix (Section 3.2.1).

3.3.2 Algorithm accuracy

Milestone #1 Accuracy Metric:

The root-mean-square of the differences of the E_{eff} and E_{ref} electric fields generated by, respectively, the efficient and reference (assumed perfectly accurate) methods measured within the annulus specified in Section 3.1.1 will represent the accuracy, in terms of contrast, of the efficient algorithm:

$$accuracy = \frac{RMS(|E_{eff} - E_{ref}|^2)}{\max(PSF)}$$

Rationale:

For each coronagraph the accuracy of the algorithm will be established relative to a reference algorithm that is assumed to be perfect, as detailed further in the appendices. How this is done depends on the coronagraph and is detailed further in the following sections. When verifying an efficient method against a more rigorous one, the computed complex-valued electric fields will be compared within the final image plane annulus described above for the same input wavefront. One field will be subtracted from the other, the modulus-squared taken, and the resulting intensity converted to contrast by dividing it by the peak unocculted stellar PSF value. In essence, this is correcting the efficient method's field (E_{eff}) using the negative of the reference field ($-E_{ref}$) and then measuring the resulting contrast.

4. Success Criteria

The following items summarize the requirements and metrics detailed in Sections 2 and 3.

4.1 The measurements to be evaluated are comparisons between the image plane monochromatic electric fields computed by the efficient models and the reference algorithms.

4.2 The fields will be computed for a wavelength of 550 nm.

4.3 The fields will be measured and compared within an annulus of $2.5 \lambda_c/D \leq r \leq 18.0 \lambda_c/D$ radians centered on the star ($\lambda_c = 550$ nm, $D =$ diameter of the entrance pupil).

4.4 Two fields will be separately evaluated, one with a mean contrast of approximately 10^{-5} and another of approximately 10^{-10} with the input aberrations scaled to provide those levels.

4.5 The RMS difference between the modeled and reference fields, expressed in terms of contrast, will be less than or equal to 1% of the mean field contrast specified in item 4.4.

4.6 The execution time required to separately propagate 2077 single monochromatic wavefronts through the chosen optical layout using the PROPER library routines and the efficient coronagraph models will be less than 48 hours on a current workstation (dual quad-core Xeon system) and will be evaluated based on the execution time of one wavefront propagation through the system.

4.7 Items 4.1 – 4.6 will be satisfied with simulations representing three different coronagraphs: Hybrid Band-Limited Coronagraph (HBLC), Vector Vortex Coronagraph (VVC), and Phase-Induced Amplitude Apodization (PIAA) coronagraph. The system optical layouts are defined in Appendix A and the coronagraphs and their respective algorithms are defined in Appendices B, C, and D.

5. Milestone Certification Data Package

The results of this study will be reported to and reviewed by NASA Headquarters. The documentation, code, and data products that provide evidence that the requirements of this milestone have been met will be:

- a. Documentation detailing the modeled optical system layout and coronagraph optical parameters.
- b. Documentation describing the efficient and rigorous algorithms used for each coronagraph.
- c. Documented computer codes (IDL, C) that implement the efficient and rigorous algorithms.
- d. Documentation detailing the accuracies achieved for the efficient algorithm for each coronagraph and the execution times necessary to create the DM response matrices.
- e. The complex-valued fields at the final image planes generated by the efficient and rigorous algorithms for each coronagraph and at each required contrast level that were used to demonstrate achievement of the milestone requirements. These will be distributed as two FITS files each (real and imaginary field components) and shown as color-coded images in the documentations.
- f. FITS files containing the input phase and amplitude error maps used to generate the results in item (e) and shown as color-coded images in the documentation.
- g. Contrast maps at each required contrast level for each coronagraph as generated by the efficient algorithms. These will be distributed as FITS files and as color-coded maps in the documentation.

At the end of Milestone #2, the efficient coronagraph modeling algorithms will be publicly released as an add-on package to the freely-available PROPER library, along with the optical system layouts.

6. References

- Balasubramanian, K. et al, "Polarization compensating protective coatings for TPF Coronagraph optics to control contrast degrading cross polarization leakage," *Proc. SPIE*, 5905 (2005).
- Belikov R., Kasdin N.J., Vanderbei R.J., "Diffraction-based Sensitivity Analysis of Apodized Pupil-Mapping Systems," *Astrophysical Journal*, 652, 833 (2006).
- Belikov, R., Pluzhnik, E., Connelley, M. S., Lynch, D. H., Witteborn, F. C., Cahoy, K., L., Guyon, O., Greene, T. P., McKelvey, M. E., "First results on a new PIAA coronagraph testbed at NASA Ames," *Proc SPIE 7440*, 74400J (2009).
- Genet, C., Ebbesen, T.W., "Light in tiny holes," *Nature*, 445, 39 (2007).
- Give'on, A., Kern, B., Shaklan, S., Moody, D., Pueyo, L., "Broadband wavefront correction for high-contrast imaging systems," *Proc. SPIE*, 6691, 66910A (2007).
- Guyon, O., Pluzhnik, E., Galicher, R., Martinache, F., Ridgeway, S., Woodruff, R., "Exoplanet Imaging with a Phase-Induced Amplitude Apodization Coronagraph. I. Principle," *Astrophysical Journal*, 622, 744 (2005).
- Kern, B. D., Belikov, R., Give'on, A., Guyon, O., Kuhnert, A. C., Levine, M. B., Moody, D. C., Jr., Niessner, A. F., Pueyo, L. A., Shaklan, S. B., Traub, W. A., Trauger, J. T., "Phase-Induced Amplitude Apodization (PIAA) coronagraph testing at the High Contrast Imaging Testbed," *Proc. SPIE*, 7440, 7440H (2009).
- Krist, J., Moody, D., Mawet, D., Trauger, J., Belikov, R., Shaklan, S., Guyon, O., Vanderbei, R., "End-to-end simulations of different coronagraphic techniques," *Proc. SPIE*, 7440 (2009).
- Krist, J., Shaklan, S., Levine, M., "Extraction of extrasolar planet spectra from realistically simulated wavefront corrected coronagraphic fields," *Proc. SPIE*, 7010, 701044 (2008).
- Krist, J., "PROPER: An optical modeling program for IDL," *Proc. SPIE*, 6675, 66750P (2007).
- Krist, J., et al., "Hunting planets and observing disks with the JWST NIRCcam coronagraph," *Proc. SPIE*, 6693, 66930H (2007).
- Krist, J., Trauger, J., Moody, D., "Studying a simple TPF-C", *Proc. SPIE*, 6265 (2006).
- Kuchner, M., Traub, W., "A Coronagraph with a Band-limited Mask for Finding Terrestrial Planets," *Astrophysical Journal*, 750, 900 (2002).
- Lieber, M., Neureuther, A., Ceperley, D., Kasdin, J., Hoppe, D., Eisenman, A., "Evaluating the end-to-end performance of TPF-C with vector propagation models: Part I – pupil mask effects," *Proc. SPIE*, 5905, 59050K (2005).
- Marois, C., Macintosh, B., Soummer, R., Poyneer, L., Mayman, B., "An end-to-end polychromatic Fresnel propagation model of GPI," *Proc. SPIE*, 7015, 70151T (2008).

- Mawet, D., et al., "Optical Vectorial Vortex Coronagraphs using Liquid Crystal Polymers: theory, manufacturing and laboratory demonstration," *Optics Express*, 17, 1902 (2009a).
- Mawet, D., Trauger, J., Serabyn, E., Moody, D., Liewer, K., Krist, J., Shemo, D., O'Brien, N., "Optical vector vortex coronagraph: first results in the visible," *Proc. SPIE*, 7440, 74400X (2009b).
- Moody, D., Gordon, B., Trauger, J., "Design and demonstration of hybrid Lyot coronagraph masks for improved spectral bandwidth and throughput," *Proc. SPIE*, 7010, 70103P (2008).
- Pluzhnik, E., Guyon, O., Ridgway, S., Martinache, F., Woodruff, R., Blain, C., Galicher, R., "Exoplanet Imaging with a Phase-Induced Amplitude Apodization Coronagraph. III. Diffraction Effects and Coronagraph Design," *Astrophysical Journal*, 644, 1246 (2006a).
- Pluzhnik, E., Guyon, O., Warren, M., Ridgway, S., Woodruff, R., "PIAA coronagraph design: system optimization and first optics testing," *Proc. SPIE*, 6265, 62653S (2006b).
- Pueyo, L., Shaklan, S., Krist, J., "Numerical propagator through PIAA optics," *Proc. SPIE*, 7440, 74400E (2009).
- Shaklan, S., "Technology Milestone #3A White Paper: Coronagraph Starlight Suppression Model Validation," JPL Document D-64582 (2009).
- Shaklan, S., Green, J., "Reflectivity and optical surface height requirements in a broadband coronagraph. 1. Contrast floor due to controllable spatial frequencies," *Applied Optics*, 45, 5143 (2006).
- Soummer, R., Pueyo, L., Sivaramakrishnan, A., Vanderbei, R., "Fast computation of Lyot-style coronagraph propagation," *Optics Express*, 15, 15935 (2007).
- Traub, W., et al., "TPF-C: status and recent progress," *Proc. SPIE*, 6268, 62680T (2006).
- Trauger, J., Stapelfeldt, K., Traub, W., Henry, C., Krist, J., et al. "ACCESS: a NASA mission concept study of an actively corrected coronagraph for exoplanet system studies," *Proc. SPIE*, 7010, 701029 (2008).
- Trauger, J., Give'on, A., Gordon, B., Kern, B., Kuhnert, A., Moody, D., et al., "Laboratory demonstrations of high-contrast imaging for space coronagraphy," *Proc. SPIE*, 6693, 66930X (2007).
- Vanderbei, R., "Diffraction Analysis of Two-dimensional Pupil Mapping for High-Contrast Imaging," *Astrophysical Journal*, 636, 528 (2006).
- Vérinaud, C., Kasper, M., Beuzit, J-L., "System study of EPICS: the exoplanets imager for the EELT," *Proc. SPIE*, 7736 (2010).
- Yaitskova, N., et al., "FOROS: Fresnel optical propagation code for SPHERE," *Proc. SPIE*, 7735 (2010).

Appendix A: Optical system layout

We assume a telescope layout identical to that used for the ACCESS mission concept study that represents a realistic system. The ACCESS telescope has a 1.5 m diameter primary mirror, which we will also assume. However, the size of the telescope will not impact the results our study, and for a larger system the components may be scaled and/or the beam feeding the coronagraph may be resized by preceding optics to keep the same instrument dimensions. The results are therefore applicable to the same coronagraphs on larger telescopes. The telescope has an off-axis Gregorian configuration that avoids the obscurations caused by a secondary mirror and its supports. The beam from the secondary is diverted behind the primary and into the coronagraph by a fold mirror. An off-axis parabola (OAP) forms a collimated beam and an image of the primary mirror on a deformable mirror (DM1). Some additional distance down the optical path a second DM (DM2) is placed to provide leverage for controlling wavefront amplitude errors. Another OAP then focuses the beam. At this point the system has two configurations, one for the HBLC /VVC (Figure 5) and another for PIAA (Figure 6):

HBLC & VVC: The occulting/OVV focal plane mask is located at the intermediate focus. An OAP then forms an image of the primary mirror on the Lyot stop, which is a simple aperture mask. Yet another OAP or lens focuses the beam onto the detector.

PIAA: The beam passes through the intermediate focus without alteration and to an OAP that collimates it and forms an image of the primary mirror on the PIAA M1 mirror. The beam is remapped onto PIAA M2 and then an OAP collimates the beam and forms an image of M2 on the post-apodizer. Another OAP focuses the beam onto the occulter. The beam is then fed directly to the first reverse PIAA mirror, M1R. This reverses the apodization produced by the forward PIAA optics, forming a geometrically undistorted wavefront on the second mirror, M2R. An OAP or lens then focuses the beam onto the detector.

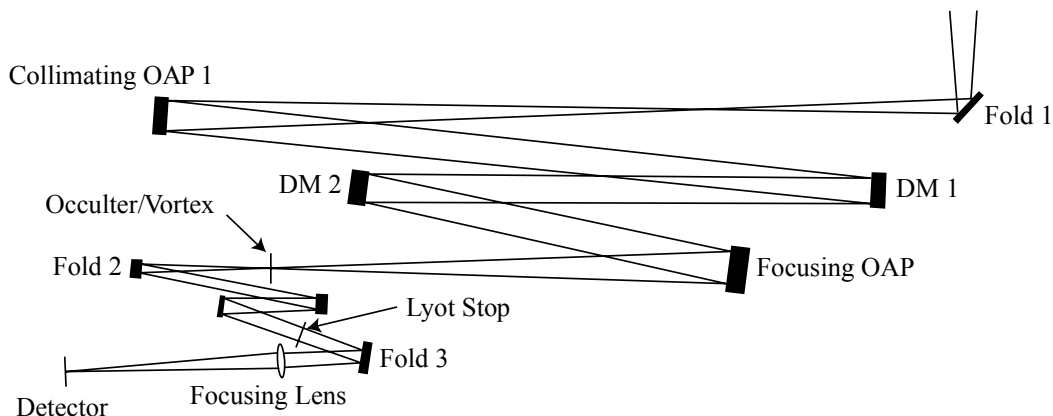


Figure 5. Schematic optical layout for the HBLC/VVC. Not shown are the telescope primary and secondary mirrors that feed Fold 1 in the upper right.

Assessing the performance limits of internal coronagraphs

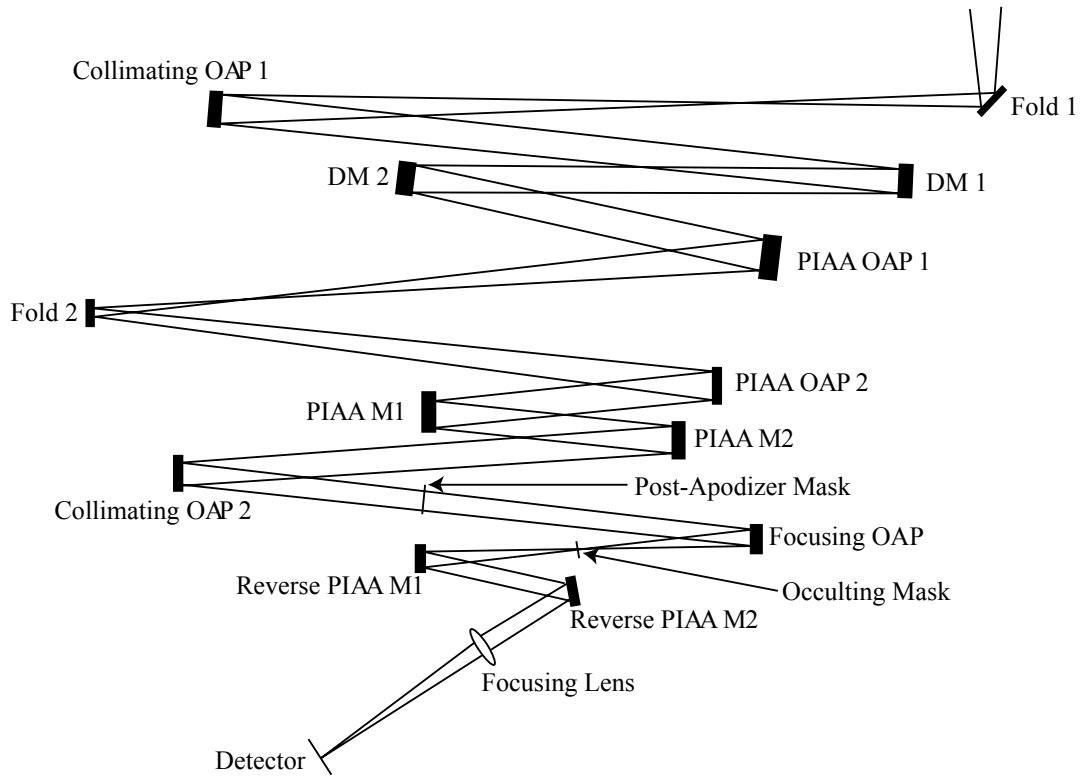


Figure 6. Schematic optical layout for the PIAA coronagraph. Not shown are the telescope primary and secondary mirrors that feed Fold 1 in the upper right.

Appendix B: PIAA modeling and verification

The surface curvature rapidly varies at the edge of the M1 optic (Figure 2). Because of the corresponding rapid phase changes and the beam remapping that occurs during propagation between the PIAA optics, it is not possible to accurately model diffraction through the system using conventional Fourier-based algorithms. Explicit computation of the Rayleigh-Sommerfeld (R-S) propagator can be used, but the time required is prohibitive for a complex, aberrated, two-dimensional input wavefront, especially when a large number of wavefronts must be processed. Another method, S-Huygens (Vanderbei 2006; Belikov et al. 2006), has been devised that achieves nearly the same accuracy as R-S, making fewer approximations than the angular spectrum method. It can be used for propagating an aberrated two-dimensional wavefront by decomposing it into one-dimensional azimuthal harmonic components (Belikov et al. 2006), each of which is separately propagated and then added together afterwards. While faster than a full R-S calculation, it is still too slow for efficient end-to-end modeling and response matrix generation. Propagation of a monochromatic, aberrated wavefront would take tens of minutes. Its accuracy, however, makes it useful as a reference against which a faster algorithm may be compared.

An efficient PIAA numerical model

The faster algorithm we propose to evaluate is the modification for PIAA of the angular spectrum propagator (hereafter PASP; Pueyo et al. 2009). The angular spectrum method is commonly used for propagation in more conventional optical systems with uniformly-sampled wavefronts, where it can be rapidly computed using two fast Fourier transforms: one to decompose the wavefront into Fourier components and another to propagate each component along with a phase term. For PIAA, the second step must be performed explicitly and so it is not as fast as the conventional method, but it is orders of magnitude faster than S-Huygens.

PASP by itself cannot adequately compute the diffraction from the edge of the M1 optic due to sampling constraints, so S-Huygens is used only along the edge to capture the effect. To do so, a weighting function is applied to the edge region of the wavefront entering M1. Previous experiments have shown that a cosine taper that is 1.0 at $0.9r$ and goes down to 0.0 at the edge ($1.0r$) is an effective weighting function (r is the pupil radius). The wavefront is multiplied by this function and the Fourier transform taken to provide the angular spectrum used by PASP. The weighting both reduces the influence of the discontinuity at the edge of the pupil to reduce spectral leakage in the transformed result and provides a means to gradually join the PASP and S-Huygens propagated wavefronts. The reverse weighting function is applied to a uniform, unaberrated pupil which is then propagated by S-Huygens (only over $0.9r - 1.0r$). The edge diffraction only has to be computed once per wavelength using S-Huygens and the result stored and used as necessary. Whether ignoring the aberrations at the very edge of the beam is important, given that much of that region will be apodized by the post-apodizer, will be evaluated in this study.

Implementation and verification of the PIAA numerical model

The steps to implement and verify the PIAA modeling code will be:

Implement and verify S-Huygens code: We have already implemented the S-Huygens algorithm as a multithreaded C-based routine called from IDL that can propagate an arbitrary input wavefront between two optical surfaces. We will verify the accuracy of this code by propagating the same simple wavefront between PIAA M1 and M2 optics using S-Huygens and a direct integration of the Rayleigh-Sommerfeld diffraction equation (which we consider exact). A grayscale post-apodizer will be applied at M2 and the wavefronts propagated via Fourier transform to a focus where the fields will be compared.

Verify the representation of a binary post-apodizer: The PASP method cannot propagate a wavefront through an explicit representation of a binary post-apodizer given the fine sampling required and must rely on an indirect representation, either a grayscale version or an analytically-derived transfer function. We will verify that the approximation and binary representation are equivalent down to a 10^{-10} contrast level by propagating a simple wavefront through both types using S-Huygens with fine sampling. Because there are no periodic or subwavelength structures in the post-apodizer, surface plasmon effects (Genet & Ebbesen 2007) are not important. Note that binary apodizers are not intended to approximate grayscale apodizers, and they cannot be compared directly to them (e.g., transmission profile scans); they are designed to control the diffraction from the edge.

Implement and verify PASP code: We will implement the PASP method in IDL (with possible calls to C code) for the defined PIAA optics. We will propagate a realistically aberrated wavefront through the system using PASP+S-Huygens and S-Huygens-only algorithms. For each, the wavefront will be defined at PIAA M1 and then propagated to PIAA M2. Using PROPER routines, the beam will then be propagated to the post-apodizer, to focus where an occulting mask is applied, and then to the reverse PIAA M1R optic. The two methods will then propagate the beam from M1R to M2R. PROPER routines will then propagate the beam to focus, where the electric fields will be measured and compared.

Because the forward PIAA propagator compresses the wavefront towards the center, low spatial frequency aberrations will become high frequency ones (Krist et al. 2009). The wavefront sampling and maximum aberration spatial frequency must be chosen to prevent aliasing that would occur during this compression. This limit will be applied to the error maps used by all three coronagraphs and must allow spatial frequencies of at least 40 cycles/D to capture folding frequency effects within the $18 \lambda_c/D$ dark hole. Likewise, aberrations on optics inside the distorted PIAA wavefront space must also be limited, as those will be compressed to higher spatial frequencies along the edge of the pupil by the reverse PIAA optics.

Appendix C: VVC modeling and verification

Owing to the vectorial nature of the phase-ramp-generating, rotationally-symmetric halfwave plate, a projection of the vectorial field onto complex scalar components is necessary if one wants to use it with scalar propagators (i.e. angular spectrum or Fresnel). Fortunately, this projection is precisely described by analytical Jones matrix formulae (see below). The projection consists of two main terms, a pure vortex component containing the geometrical phase ramp $e^{i\ell\theta}$ and a so-called chromatic leakage term that produces no phase modification. The pure vortex term $e^{i\ell\theta}$ is challenging to represent numerically on a finite grid due to its intrinsic rapid phase variations close to the center (the center is a singularity). Special aliasing considerations and sampling tricks need to be considered.

Derivation of the vector vortex coronagraph analytical representation

The full rigorous analytical polarization analysis of the VVC is best performed using the Jones matrix formalism in polar coordinates (because of the intrinsic rotational symmetry of the VVC). The VVC focal plane mask is a rotating halfwave plate that is described by the following Jones matrix product:

$$J_{VVC}(r, \theta, \lambda) = M[\varphi(r, \theta)] * HWP(r, \theta, \lambda) * M[\varphi(r, \theta)]^{-1}$$

where the imperfect halfwave plate is described by

$$HWP(r, \theta, \lambda) = \begin{bmatrix} s(r, \theta, \lambda)e^{-i\Delta\phi(r, \theta, \lambda)/2} & 0 \\ 0 & p(r, \theta, \lambda)e^{+i\Delta\phi(r, \theta, \lambda)/2} \end{bmatrix}$$

with s and p being the transmitted amplitude coefficients for the local orthogonal s and p polarization components, and $\Delta\phi$ is the retardance introduced by the HWP between those components. For a perfect HWP, $s = p = 1$ and $\Delta\phi = \pi$. The φ -dependent rotation matrix is

$$M[\varphi(r, \theta)] = \begin{bmatrix} \cos \varphi(r, \theta) & -\sin \varphi(r, \theta) \\ \sin \varphi(r, \theta) & \cos \varphi(r, \theta) \end{bmatrix}$$

The angle $\varphi(r, \theta)$ parameterizes the local orientation of the optical axis of the HWP.

Before doing the matrix multiplication, let us use a common coordinate system transform, switching the polarization basis from linear to circular (sometimes called helical). This coordinate transform is common and perfectly valid. The helical transformation matrix is

$$U = \frac{1}{\sqrt{2}} \begin{bmatrix} 1 & i \\ 1 & -i \end{bmatrix}$$

The transform is then performed as follows to create the Jones matrix:

$$\begin{aligned} J_{VVC}^{LR}(r, \theta, \lambda) &= U * J_{VVC}(r, \theta, \lambda) * U^{-1} \\ &= \begin{bmatrix} L(r, \theta, \lambda) & V(r, \theta, \lambda)e^{i2\varphi(r, \theta)} \\ V(r, \theta, \lambda)e^{-i2\varphi(r, \theta)} & L(r, \theta, \lambda) \end{bmatrix} \\ &= \begin{bmatrix} L(r, \theta, \lambda) & V(r, \theta, \lambda)e^{i\theta} \\ V(r, \theta, \lambda)e^{-i\theta} & L(r, \theta, \lambda) \end{bmatrix} \end{aligned}$$

where L is the so-called chromatic leakage,

$$L(r, \theta, \lambda) = \frac{1}{2} [s(r, \theta, \lambda) + p(r, \theta, \lambda)e^{i\Delta\phi(r, \theta, \lambda)}]$$

and V is the pure vortex weighing coefficient,

$$V(r, \theta, \lambda) = \frac{1}{2} [s(r, \theta, \lambda) - p(r, \theta, \lambda)e^{i\Delta\phi(r, \theta, \lambda)}].$$

Note that the topological charge l is defined such as $\varphi(r, \theta) = l\frac{\theta}{2}$.

From the vectorial representation to the scalar model

Natural unpolarized or partially polarized light can always be decomposed into two mutually incoherent, orthogonal linear (s and p) or circular (L and R), components. Therefore, a full vector representation of the incoming aberrated wavefront consists of two scalar complex fields, $W_s(r, \theta, \lambda)$ and $W_p(r, \theta, \lambda)$, or $W_L(r, \theta, \lambda)$ and $W_R(r, \theta, \lambda)$, according to the chosen basis. The effect of the VVC on the impinging vectorial field is then described by the space-variant, wavelength-dependent Jones matrix given above.

The matrix J rigorously captures the full polarization characteristics of the VVC in the helical basis (with left L and right R circular polarization components). It links the input wavefront complex fields W_L and W_R to their respective state at the output of the VVC with a simple matrix multiplication

$$\begin{bmatrix} W_L^o(r, \theta, \lambda) \\ W_R^o(r, \theta, \lambda) \end{bmatrix} = \begin{bmatrix} L(r, \theta, \lambda) & V(r, \theta, \lambda)e^{i\theta} \\ V(r, \theta, \lambda)e^{-i\theta} & L(r, \theta, \lambda) \end{bmatrix} \times \begin{bmatrix} W_L^i(r, \theta, \lambda) \\ W_R^i(r, \theta, \lambda) \end{bmatrix}$$

Any retardance ($\Delta\Phi$) or axis-dependent throughput defect (s and p) of the rotating HWP can be rigorously represented as a perturbation of the complex leakage term L , which is chromatically and spatially dependent:

$$L(r, \theta, \lambda) = \frac{1}{2} [s(r, \theta, \lambda) + p(r, \theta, \lambda)e^{i\Delta\phi(r, \theta, \lambda)}]$$

Those defects are caused by the intrinsic properties of the LCP coating. For instance the local retardance $\Delta\Phi$ is fixed by the thickness of the LCP layer and its wavelength dependent birefringence. The throughput depends on the same intrinsic properties of the LCP layer plus its interaction with the surrounding media (substrates). A rigorous representation of the VVC can be obtained by predicting the constituent of the leakage term very precisely from as-designed devices using thin-film calculations for multi-layer coatings. Resulting maps of axis-dependent throughput and retardance defects can be injected into the VVC formula and then transferred to the output wavefronts W_L and W_R .

Implementation and verification of the VVC numerical model

A rigorous diffraction analysis of the VVC requires the propagation of the vortex equation terms independently from one another, meaning 4 different mutually-incoherent propagations (in reality 3, since the 2 leakage terms are strictly identical). The results of those 4 propagations need to be added incoherently.

In the efficient model, it is expected and it will be verified that the full propagation of the Jones matrix is not required since the dominant term is V . Note that the phase ramps are conjugated, so again a separate propagation is not necessary. At the end, an efficient representation of the VVC can be limited to the propagation of a single term of the Jones matrix.

An accurate representation of the phase ramp necessitates supersampling of the central region of the vortex, opaque mask included, where the phase and amplitude rapidly change over a relatively limited number of pixels. This is also where most of the light is. This supersampling trick has been known for quite a long time. It involves computing the central region phase ramp on an array that is X times bigger than the region per se, and then rebinning the big array in complex space down to normal sampling, and inserting this new array into the original VVC phase ramp array.

This can be verified against an overly sampled propagation using extreme-sized arrays (e.g. 16K×16K pixels with 40× PSF oversampling). While computationally intensive, this verification needs only be done once in a perfect case and for a limited number of aberrated wavefronts, and checked against the supersampled version of it with more reasonably sized propagation arrays (e.g., 2K×2K, with 5× PSF oversampling).

A “super-model” of the VVC will be generated based on a realistic model of the LCP rotating halfwave plate projected on a highly oversampled grid (16K×16K) for propagation. This will allow us to capture all polarization effects down to fine spatial scales. This “super-model” will be checked against the efficient model based on the “reduced” Jones matrix model, on a reasonably sized array.

The fineness of the sampling will be judged against the analytical model. It is relatively easy since in the perfect case, where the contrast is infinite, the spacing would be zero. The goal is to approach that value as closely as possible. In practice, the threshold will be a couple orders of magnitude below the goal contrast level 10^{-10} . We will iteratively decrease the sampling until convergence is achieved or we exceed the required contrast.

We previously implemented a propagator using the Discrete Fourier Transform (DFT) method (Soummer et al. 2007), but it does not appear to work for the pure VVC. The need to restrict the phase spiral to the central part using this technique creates an artificial boundary where the representation is discontinuous. Soummer et al. (2007) explicitly mention that the method is only applicable to Lyot-type coronagraphs with a finite extension in the focal plane. However, the Soummer et al. method can be used to refine the representation of the central spot, which is finite. Indeed, the hybrid VVC (VVC with the central opaque spot) can be considered as the difference of the perfect VVC and a finite VVC, whose size corresponds to the central spot. The pure infinite VVC is treated as mentioned earlier, with a clear analytical solution as a gauge to define the optimal sampling. For the finite VVC, we are only interested in computations inside limited areas, i.e., the limited occulting mask area and the limited Lyot stop area. We can thus completely circumvent the sampling problem by restricting the use of the transforms to these two zones. We need to compute these limited-area transforms and subtract the result from the pupil complex amplitude. In the general two-dimensional case, the two limited-area transforms can be calculated using partial Fourier methods. Several methods exist to calculate such partial these, such as the Fractional Fourier Transform.

Appendix D: HBLC modeling and verification

The HBLC involves phase modification by dielectric coatings and amplitude modification by an absorbing layer, both of which can be computed using thin film calculations that directly apply Maxwell's equations. We will utilize thin-film software that has been in use since the early 1970's and which we assume to be exact (it is just applying Maxwell's equations).

The wavefront modification by the DMs is dependent on propagation through the system and we will rely on the PROPER algorithms. The accuracy of these routines will be demonstrated by propagating the same aberrated wavefront through an HBLC system using PROPER and S-Huygens (whose accuracy will be demonstrated in the PIAA modeling verification process).